RSC Advances

PAPER

View Article Online
View Journal | View Issue

Cite this: *RSC Adv.*, 2026, **16**, 20526

Diethylenetriamine-driven assembly of a dimeric cadmium bromide hybrid and an organic bromide salt: structural, vibrational, optical, *in silico* study and biological insights

Iteb Ben Mahmoud,[a] Mashael A. Alghamdi,[b] Houda Lazreg Aref,[c] Noureddine Mhadhbi,[ad] Hossam H. Nasrallah,[e] Ahlem Guesmi,[b] Naoufel Ben Hamadi,[b] Sandra Walha,[a] Ferdinando Costantino[f] and Houcine Naïli *[a]

Diethylenetriamine (DET) was employed to synthesize two novel crystalline materials: a cadmium-based hybrid, $(C_4H_{16}N_3)[CdBr_5]\cdot H_2O$ (DETCdBr), and an organic salt, $(C_4H_{16}N_3)Br_3$ (DETBr). Single-crystal X-ray diffraction reveals that both crystallize in the monoclinic space group $P2_1/c$, with DETCdBr featuring $[Cd_2Br_{10}]^{6-}$ dimeric units constructed from corner-sharing $CdBr_6$ octahedra, while DETBr consists of discrete ionic moieties stabilized by N–H···Br interactions. Complementary analyses (PXRD, SEM, FTIR, and Hirshfeld surface) confirm structural features, phase purity, and the dominant role of hydrogen bonding in both systems. Complementary *in silico* studies, including DFT calculations, ADME predictions, and molecular docking, confirm the electronic stability, reactive sites, and enzyme-binding potential of DETBr and DETCdBr. DETBr exhibits drug-like electronic properties with high solubility and favorable α-amylase interactions, while DETCdBr benefits from the cadmium scaffold, enhancing electrostatic and hydrogen-bonding contacts. Optical studies reveal a significant contrast: DETBr exhibits deep-UV absorption, whereas DETCdBr shows an extended absorption into the visible region with a reduced band gap (~2.85 eV), attributed to metal–halide charge-transfer transitions. Both compounds display white-light photoluminescence with CIE coordinates near (0.32, 0.34) for DETCdBr and (0.30, 0.32) for DETBr. Biological assays demonstrate that both compounds inhibit α-amylase through distinct mechanisms: DETBr acts as a competitive inhibitor, while DETCdBr exhibits non-competitive behavior, highlighting the influence of structural organization on biological activity. These findings underline the role of metal coordination in tuning structural, optical, and functional properties.

Received 3rd April 2026
Accepted 13th April 2026

DOI: 10.1039/d6ra02827f

rsc.li/rsc-advances

1 Introduction

The field of organic–inorganic hybrid materials has been growing intensively during the past 20 years and is certainly nowadays one of the major fields of research and unambiguously one of the most exciting. The idea of combining organic and inorganic systems has now gained strong support. However, due to the complexity of designing associations between materials that exhibit very low mutual compatibility, chemists and physicists have been led to envision numerous architectures, more or less easy to achieve experimentally. The rising of new characterization techniques and knowledge at the nanometer scale and even the molecular scale has been a driving force towards imagination of hybrid architectures in many major fields such as sensors, electronics, optics, lightning, medicine, catalysis, energy storage, energy conversion.[1–12]

The unique chemical behavior of metal ions with a full d^{10} electron shell, such as Cd(II), makes them excellent building blocks in coordination chemistry.[13–15] For this reason, cadmium has become a metal of significant interest, particularly in the development of new coordination materials.[16,17] Owing to this distinctive electronic configuration, Cd^{2+} exhibits remarkable flexibility in its coordination behavior.[18,19] Its complexes are known for their dynamic nature, allowing facile ligand exchange and structural rearrangement, which in turn makes cadmium an attractive choice for constructing diverse

[a]*Laboratory Physical-Chemistry of the Solid State, Department of Chemistry, Faculty of Sciences of Sfax, BP 1171, Sfax 3000, University of Sfax, Tunisia. E-mail: houcine_naili@yahoo.com*

[b]*Chemistry Department, College of Science, Imam Mohammad Ibn Saud Islamic University (IMSIU), Riyadh 11623, Saudi Arabia*

[c]*University of Monastir, Higher Institute of Biotechnology of Monastir, Laboratory of Genetics, Biodiversity and Bioresources Valuation LR11S41, 5019 Monastir, Tunisia*

[d]*University of Monastir, Preparatory Institute for Engineering Studies of Monastir, Monastir 5019, Tunisia*

[e]*Chemistry Department, Faculty of Biotechnology, Sinai University, Kantara 41632, Egypt*

[f]*Department of Chemistry Biology and Biotechnologies, University of Perugia, Via Elce di Sotto 8, 06123 Perugia, Italy*

molecular architectures and coordination polymers. This structural adaptability not only broadens the range of possible coordination modes but also directly influences the resulting physical properties of these compounds. Its tendency to form stable yet versatile bonds with a wide variety of organic ligands has inspired extensive research into Cd(II)-based systems, spanning from discrete multinuclear clusters to extended polymeric frameworks.[20] Such diversity in coordination environments often gives rise to intriguing structural motifs and notable photo-physical properties.[21,22] Consequently, cadmium continues to draw considerable scientific attention, not only for its structural versatility but also for its potential in developing materials with distinctive optical and electronic behaviors.[23–26]

In the present work, diethylenetriamine (DET) was chosen as the nitrogen-donor ligand to explore its coordination behavior toward cadmium in the synthesized compound DETCdBr, and to compare its structural role with that in the organic salt DETBr. Owing to its molecular structure, which contains two terminal primary amine groups and one central secondary amine group, DET offers multiple coordination sites capable of binding metal centers in diverse modes. This characteristic allows it to act either as a terminal or bridging ligand, potentially influencing the geometry and dimensionality of the resulting framework.[27] Through a combination of structural, morphological, spectroscopic, and biological analyses, we show how the presence of cadmium fundamentally alters the crystal packing, optical behavior, and enzyme inhibition mechanism.

2 Experimental section

2.1. Synthesis

All the employed chemicals, hydrobromic acid (HBr; 48%), cadmium bromide tetrahydrate ($CdBr_2 \cdot 4H_2O$; 98%) and diethylenetriamine ($(NH_2CH_2CH_2)_2NH$; 99%) were commercial products (Sigma-Aldrich), which were used without further purification. The two new hybrid salts DETCdBr and DETBr were synthesized by the slow evaporation method.

The title compound DETCdBr was synthesized by the reaction of diethylenetriamine (2 mmol: 0.206 g), cadmium bromide tetrahydrate (1 mmol: 0.344 g) and 10 mL of distilled water. The compound DETBr was synthesized by combining diethylenetriamine (2 mmol: 0.206 g) with 10 mL of distilled water. The resulting solutions were acidified with concentrated hydrobromic acid (1 mmol; 5 drops). The mixtures were then stirred magnetically for 15 minutes at room temperature, leading to the formation of homogeneous solutions. A few days later, some crystals of a size suitable for structural study were obtained. The product is then filtered, washed with a minimum of distilled water and air dried. Elemental microanalysis confirmed the composition of our new materials, giving the following values: calculated: C, 7.02%; H, 2.65%; N, 6.14%. Found: C, 6.98%; H, 2.71%; N, 6.08% for DETCdBr and calculated: C, 12.97%; H, 4.35%; N, 11.34%. Found: C, 13.02%; H, 4.28%; N, 11.41% for the other compound. The synthesis process of DETCdBr is illustrated in Scheme 1.

2.2. Micrographs and X-ray microanalysis

The morphology of the synthesized compounds, DETCdBr and DETBr, was examined using scanning electron microscopy (SEM) on a JEOL-6610LV instrument operated at an accelerating voltage of 20 kV. The system was equipped with an Oxford X-Max energy-dispersive X-ray (EDX) detector, which was employed to analyze the elemental composition and assess the crystal shape and surface features of both materials.

2.3. X-ray powder diffraction

The powder X-ray diffraction (PXRD) pattern of DETCdBr was recorded in reflection geometry over a 2θ range of 5–50°, with a step size of 0.025°, using a Bruker D8 Advance diffractometer equipped with a LYNXEYE XE-T detector and a Cu Kα radiation source. The ceramic tube was operated at 40 kV and 40 mA.

PXRD measurements under controlled atmosphere were additionally carried out using a PANalytical X'Pert diffractometer in transmission geometry, employing Cu Kα radiation and an X'Celerator strip detector.

2.4. X-ray data collection

A single colorless block-shaped crystals of DETCdBr (**1**) and DETBr (**2**) were selected for data collection. Each suitable crystal was mounted on a MITIGEN holder in perfluoroether oil and measured on a XtaLAB Synergy, Dualflex, HyPix-Arc 100 diffractometer. Both structures were solved using the ShelXT 2018[28] solution program with dual methods and refined in Olex2.[29] Final refinements were carried out with ShelXL 2018[30] using full matrix least squares minimization on F^2. All non-hydrogen atoms were refined anisotropically.

Hydrogen atoms bonded to carbon and nitrogen were positioned geometrically and refined using a riding model, with fixed C–H and N–H bond lengths of 0.99 Å and 0.91 Å, respectively. The hydrogen atoms of the water molecules were located from difference Fourier maps and refined with isotropic displacement parameters.

The main crystallographic data and refinement parameters of the two compounds (**1**) and (**2**) are summarized in Table S1. The molecular graphics were prepared using the Diamond 3 software.[31]

2.5. Hirshfeld surface analysis and fingerprint plots

Hirshfeld surface analysis was conducted to visualize and quantify the intermolecular interactions present in the crystal structure of DETCdBr. The three-dimensional Hirshfeld surfaces and the corresponding two-dimensional fingerprint plots were generated using the Crystal Explorer program.[32]

2.6. FT-IR spectroscopy

The infrared (IR) spectrum was recorded at room temperature using a PerkinElmer BX spectrometer. The sample was prepared using the conventional KBr pellet technique, and the spectrum was collected in the 400–4000 cm^{-1} wavenumber range. Meanwhile, the optical absorption spectra of the films were recorded at room temperature using a UV-visible

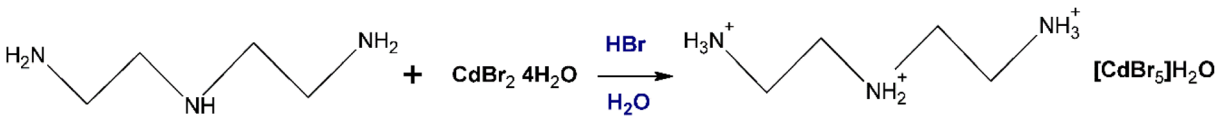

Scheme 1 Schematic representation of the synthesis of the DETCdBr complex.

spectrophotometer (Cary 4000, Version 2.24) over the wavelength range of 200–800 nm.

2.7. *In silico* studies

Density Functional Theory (DFT) calculations were carried out using the B3LYP/6-31G(d) level of theory. Optimized geometries were used to analyze frontier molecular orbitals (HOMO/LUMO), energy gaps (ΔE), and molecular electrostatic potential (MEP) maps, providing insight into electronic structure, reactivity, and potential interaction sites, complementing docking and pharmacokinetic predictions.[33–35]

The drug-likeness, pharmacokinetic properties, and physicochemical characteristics of DETBr and DETCdBr were predicted using SwissADME online platform.[36] Canonical SMILES strings were used to calculate molecular weight, lipophilicity (log *P*), hydrogen bond donors/acceptors, and topological polar surface area (TPSA). Drug-likeness was evaluated according to Lipinski's rule of five, as well as Veber and Ghose criteria. Predicted pharmacokinetic parameters included gastrointestinal absorption, blood–brain barrier permeability, P-glycoprotein substrate recognition, and cytochrome P450 enzyme inhibition profiles.

Additionally, molecular docking studies were performed to investigate ligand–α-amylase interactions (PDB ID: 4W93).[37,38] The protein structure was prepared by removing water molecules and co-crystallized ligands, followed by the addition of polar hydrogens and assignment of Kollman charges. Ligand geometries were energy-minimized using Chem3D, with appropriate charge assignment and definition of rotatable bonds.

For the metal-containing complex, the ligand structure was derived from the experimental CIF file to preserve the accurate coordination environment. Docking simulations were carried out using AutoDock Vina, with the grid box centered on the catalytic residues Trp59, Glu63, and Asp300. The best binding poses were selected based on binding affinity and detailed interaction analysis, including hydrogen bonding, electrostatic interactions, and hydrophobic contacts.[39–41]

2.8. Biological activity evaluation

2.8.1. Assessment of α-amylase inhibition by DETBr and DETCdBr. The inhibitory potential of DETBr and DETCdBr toward α-amylase was assessed using a slightly modified colorimetric method based on previously published procedures.[42] Porcine pancreatic α-amylase was dissolved in 10 mM phosphate buffer (pH 6.9) to reach a final concentration of 1 mg mL^{-1}. A starch substrate solution (1%, w/v) was prepared in phosphate-buffered saline and heated in boiling water for 15 minutes to ensure complete gelatinization. The solution was then cooled to room temperature before use.

Test solutions of DETBr and DETCdBr were prepared in phosphate buffer at concentrations ranging from 0.25 to 2 mg mL^{-1}. For each assay, 20 μL of the sample solution was mixed with 20 μL of the enzyme solution and pre-incubated at 37 °C for 15 minutes. The enzymatic reaction was initiated by adding 100 μL of the starch solution, and the mixture was incubated for an additional 5 minutes at 37 °C.

The reaction was terminated by adding 0.5 mL of dinitrosalicylic acid (DNS) reagent, followed by heating in a boiling water bath for 15 min to allow color development. After cooling to room temperature, 1.5 mL of distilled water was added, and the absorbance was measured at 540 nm using a UV-visible spectrophotometer. A glucose solution (1 g L^{-1}) was used to generate the calibration curve, while acarbose served as the reference inhibitor.

The percentage of enzyme inhibition was calculated using the following equation:

$$\text{Inhibition } (\%) = \frac{A_{\text{control}} - A_{\text{sample}}}{A_{\text{control}}} \times 100$$

where A_{control} represents the absorbance measured without inhibitor and A_{sample} corresponds to the absorbance obtained in the presence of DETBr or DETCdBr.

2.8.2. Evaluation of kinetic parameters and mode of enzyme inhibition. The kinetic properties of α-amylase in the presence and absence of DETBr and DETCdBr were analyzed using Lineweaver–Burk double-reciprocal plots derived from the Michaelis–Menten model.[43] This graphical approach enabled the determination of the maximum reaction velocity ($V_{\max}$) and the Michaelis constant (K_m).

The inhibition mechanism was identified by comparing the variations in K_m and $V_{\max}$ values obtained in the presence of the tested samples. Double-reciprocal plots were constructed by plotting the reciprocal of substrate concentration against the reciprocal of reaction velocity.

Furthermore, the inhibition constant (K_i) was calculated according to the inhibition model determined from the kinetic analysis. This constant provides additional information regarding the affinity between α-amylase and the investigated inhibitors.

3 Results and discussions

3.1. SEM and EDX characterization of DETCdBr and DETBr

The SEM micrographs in Fig. 1a and b reveal the morphological features of the DETCdBr compound. At magnifications of ×6k and ×15k, the images show densely packed and highly

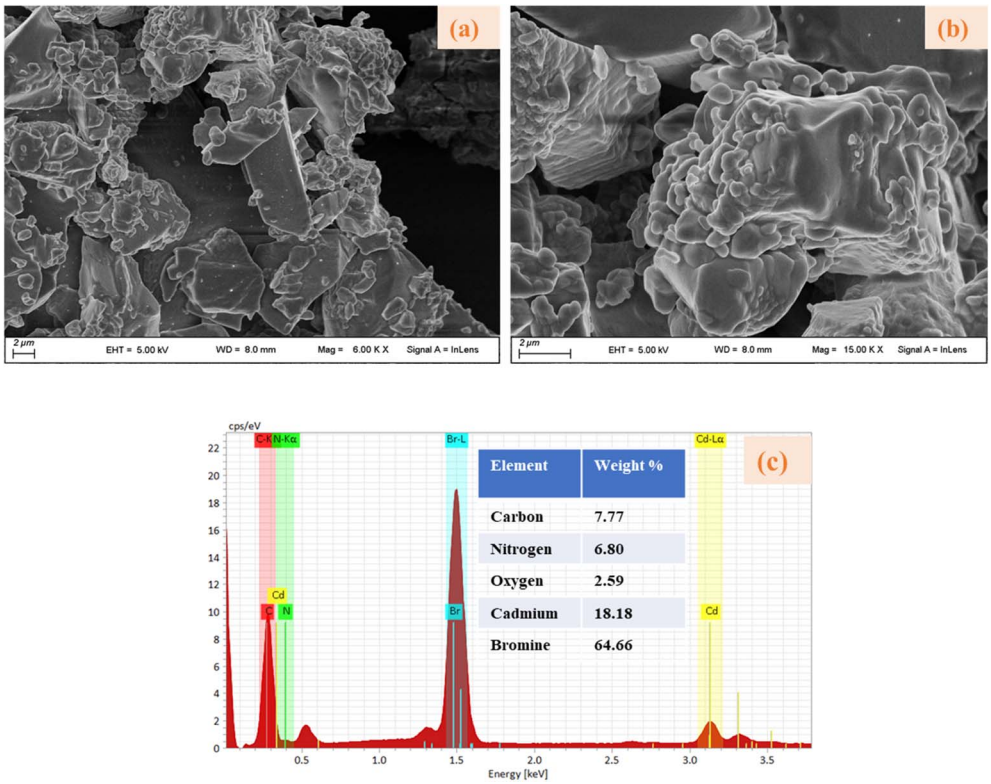

Fig. 1 Crystal morphology and scanning electron microscopy (a and b) alongside with a energy-dispersive X-ray (EDX) spectrum (c) of DETCdBr.

agglomerated crystalline particles, forming a compact microstructure with very low porosity. The material exhibits a high degree of densification, with crystal fragments displaying sharp and well-defined edges that appear partially fused into rigid aggregates. Slight variations in particle size and shape are observed across the surface; however, the overall morphology remains homogeneous and tightly packed. This compact arrangement can be attributed to the presence of an extended inorganic–organic hybrid framework, where the $[Cd_2Br_{10}]^{6-}$ dimeric units are strongly interconnected with the organic cations through electrostatic interactions and hydrogen bonding, leading to enhanced structural cohesion. The EDX spectrum (Fig. 1c) confirms the presence of the expected elements, namely carbon (C), nitrogen (N), cadmium (Cd), and bromine (Br), in agreement with the chemical composition of the compound.

By comparing the experimental PXRD pattern of DETCdBr with the simulated pattern derived from single-crystal data (Fig. 2), it was possible to confirm that the compound crystallizes as a pure phase. The positions of the experimental diffraction peaks are in good agreement with the calculated ones, indicating the absence of detectable secondary phases or impurities. Moreover, the relative intensities of the main reflections closely match the theoretical pattern, further supporting the high crystallinity and phase purity of the synthesized material.

In contrast, the morphology of the DETBr compound (Fig. 3a), recorded at a higher magnification of ×115k, clearly differs from that of DETCdBr. The microstructure is composed of smaller, irregularly shaped crystalline particles that are only moderately agglomerated, resulting in a less compact and more porous architecture. The surface exhibits a lower degree of densification, with grains characterized by smoother contours and less-defined edges, indicating weaker particle cohesion and a more flexible structural organization. This behavior reflects the absence of an extended inorganic framework, as the structure of DETBr is governed primarily by electrostatic interactions

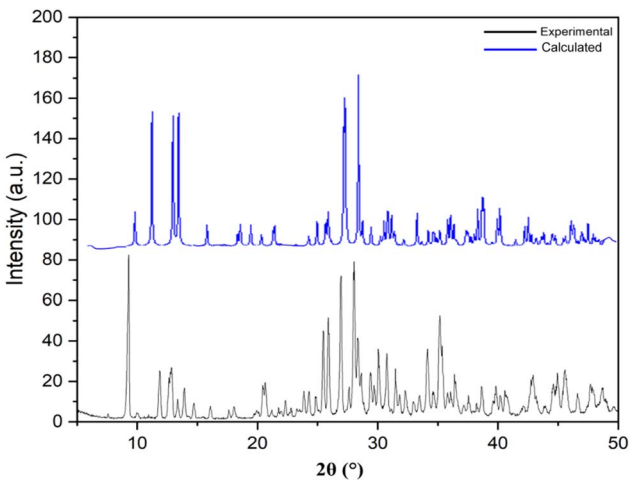

Fig. 2 Comparison of calculated and experimental XRD patterns for $(C_4H_{16}N_3)[CdBr_5]\cdot H_2O$.

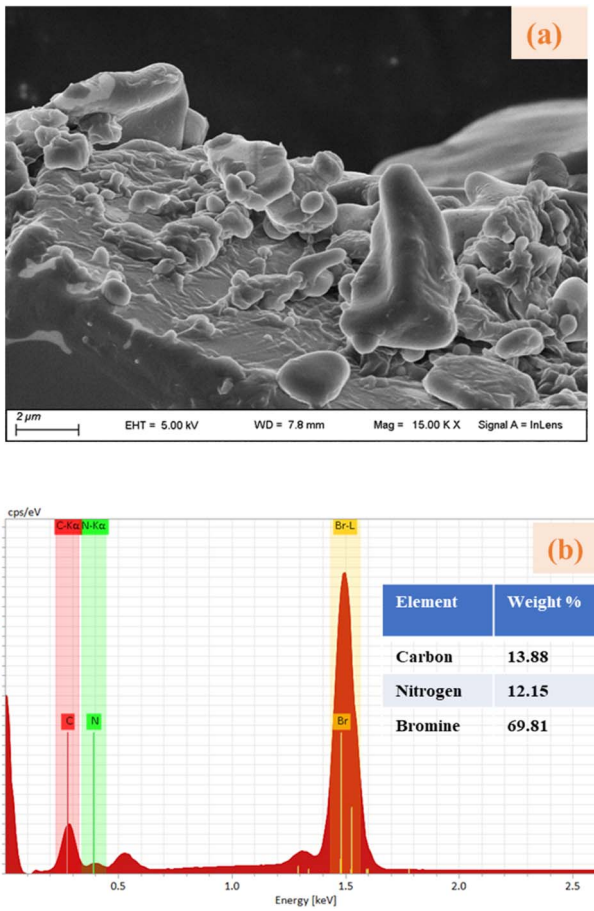

Fig. 3 (a) Crystal morphology and scanning electron microscopy (b) energy-dispersive X-ray (EDX) spectrum of DETBr.

between triprotonated diethylenetriamine cations and bromide anions, along with N–H···Br hydrogen bonding. Such interactions lead to a more open supramolecular arrangement with increased surface accessibility. The EDX analysis (Fig. 3b) further confirms the presence of carbon (C), nitrogen (N), and bromine (Br), consistent with the composition of the organic salt.

3.2. Structural investigations of $(C_4H_{16}N_3)[CdBr_5]\cdot H_2O$ and $(C_4H_{16}N_3)Br_3$

A comprehensive elucidation of the crystal structure is essential for understanding the properties and potential applications of the novel hybrid materials DETCdBr and DETBr. We have successfully synthesized these compounds, both characterized by a crystalline structure in the monoclinic crystal system with space group $P2_1/c$. In DETCdBr, an inversion center is located on the $[Cd_2Br_{10}]^{6-}$ dimer, so the asymmetric unit contains only half of the full formula unit ($Z_0 = 1$), while the unit cell accommodates four complete formula units ($Z = 4$). The refined cell parameters are $a = 10.3311(3)$ Å, $b = 10.4970(2)$ Å, $c = 14.6429(3)$ Å, with $\beta = 110.462(3)°$ (Table S1). Fig. 4, produced with DIAMOND 3, illustrates the complete formula unit of DETCdBr. The latter is composed of two triprotonated organic

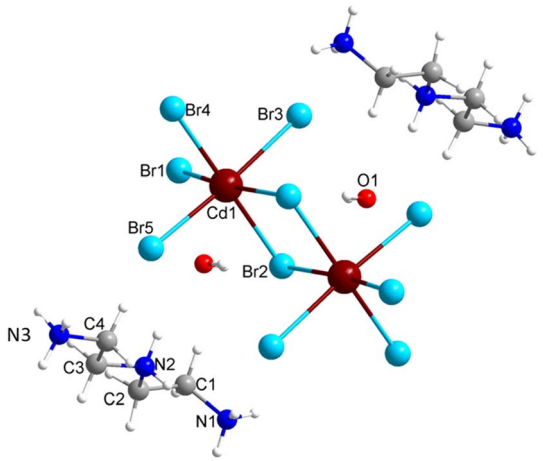

Fig. 4 The formula unit of $(C_4H_{16}N_3)_2[Cd_2Br_{10}]\cdot 2H_2O$.

cations $(C_4H_{16}N_3)^{3+}$, one $[Cd_2Br_{10}]^{6-}$ dimer, and two water molecules.

The crystal structure consists of dimeric inorganic octahedra assembled into layers extending along the [101] direction, with organic cations occupying the interlayer spaces (Fig. 5a). Each cadmium atom is octahedrally coordinated by six bromine atoms. The Cd–Br bond lengths range from 2.7422(6) to 2.8462(2) Å, while the Br–Cd–Br bond angles vary between 83.462(16)° and 176.362(18)° (Table S2). Neighboring octahedra share edges *via* μ_2-Br bridges, forming $[Cd_2Br_{10}]^{6-}$ dimeric units (Fig. 5b). Each dimer consists of two cadmium centers, linked through symmetric μ_2-bridging bromine atoms, Br2 and Br2^i, where each Br2 atom occupies an equatorial position in one octahedron and bridges to the adjacent metal center. The remaining bromine atoms, Br1, Br3, Br4, and Br5, occupy terminal positions. This layered structural motif is consistent with related compounds with different metals and dimensionalities.[44–46]

The degree of structural distortion in the $[CdBr_6]$ octahedron is quantified using the distortion parameter Δd, defined by:

$$\Delta d = \frac{1}{6}\sum_{n=1}^{6}\left(\frac{d_n - d}{d}\right)^2$$

where d is the average Cd–Br bond length (2.784 Å) and d_n refers to the individual Cd–Br bonds in the octahedra. While the calculated Δd gives a value of 2.4×10^{-4}, proving that $[CdBr_6]$ octahedron is nearly regular, with only a slight deviation from ideal geometry in comparison with other octahedron in 1D structures such (4-BAPC) ($\Delta d = 1.059 \times 10^{-3}$),[45] $(mpz)_2PbBr_{10}$ ($\Delta d = 4.5 \times 10^{-4}$),[47] and α-(DMEN)$PbBr_4$ ($\Delta d = 1.7 \times 10^{-3}$).[48]

The organic cations are interspersed between the discrete $[Cd_2Br_{10}]^{6-}$ dimeric units, which are oriented such that their terminal primary ammonium groups act as hydrogen-bond donors toward the bromide anions. The supramolecular hydrogen-bonding network of the compound is illustrated in Fig. 6 where the interstitial water molecules participate actively in the hydrogen-bonding scheme, connecting the inorganic and organic sublattices by forming O–H···Br and O–H···N bridges

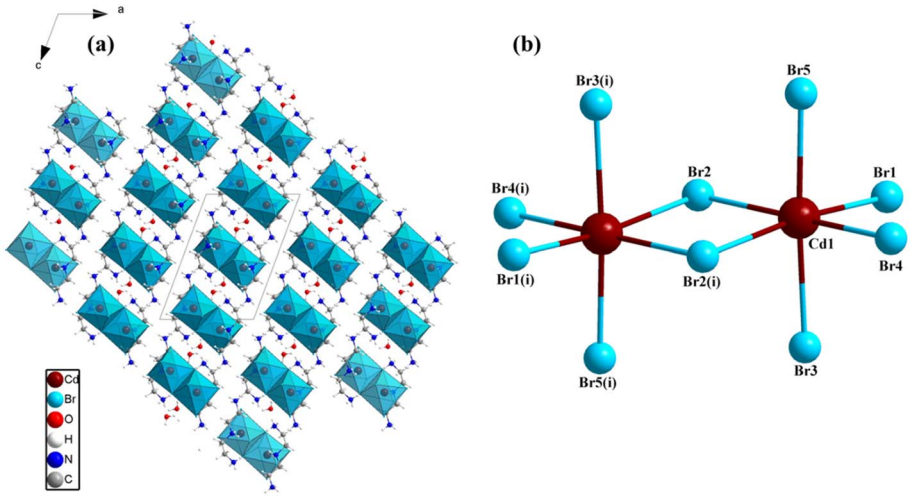

Fig. 5 (a) View of the DETCdBr framework along the *b*-axis. (b) Geometric representation of the $[Cd_2Br_{10}]^{6-}$ dimer, highlighting the different Cd–Br bond lengths. Symmetry code: (i) $1-x, 1-y, 1-z$.

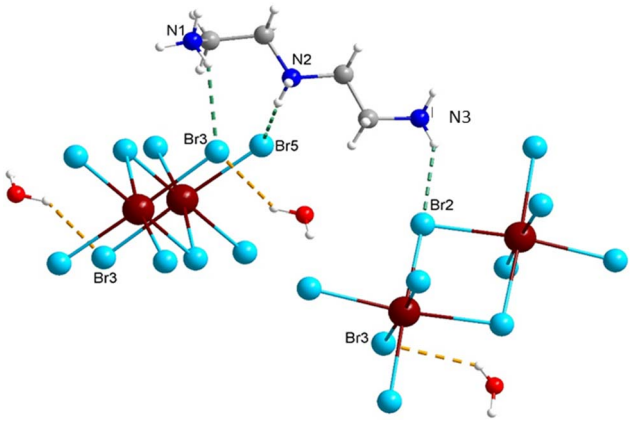

Fig. 6 Hydrogen bonds in the compound DETCdBr.

(Table S3). Therefore, these interactions play a crucial role in the structural stabilization.

In the other hand the corresponding molecular structure of DETBr is presented in Fig. 7. It crystallizes in the monoclinic crystal system with the centrosymmetric space group $P2_1/c$. The asymmetric unit consists of one organic cation, $[C_4H_{16}N_3]^{3+}$, and three bromide anions that are distributed around it through a network of non-covalent interactions (Fig. 7a). The organic moiety adopts an extended conformation, in which the carbon–nitrogen chain displays a nearly linear geometry, favoring the formation of multiple hydrogen bonds with the halide ions.

As illustrated in Fig. 7b, the three bromide anions act as acceptors in several N–H···Br hydrogen bonds, generating a three-dimensional supramolecular network. These hydrogen-bonding interactions play a key role in stabilizing the structure and in linking neighboring cations into infinite chains running approximately along the [010] and [001] directions. The overall packing can thus be viewed as an organic–halide framework sustained by moderately strong N–H···Br hydrogen bonds, which is typical of halogen-containing organic salts (Table S4).

This supramolecular arrangement suggests that electrostatic and hydrogen-bonding interactions dominate the crystal cohesion, consistent with the aliphatic nature of the DET cation. The resulting network contributes to the structural rigidity of the compound and likely influences its optical and thermal properties, as observed in similar organic halide systems.[49,50]

3.3. Hirshfeld surface analysis for DETCdBr and DETBr

The Hirshfeld surface is a valuable tool for visualizing and analyzing the intermolecular interactions that define molecular packing within a crystal structure. In this work, d_{norm}, shape index, curvedness and 2D fingerprint was carried out for both DETCdBr and DETBr compounds, and the resulting surfaces are illustrated in Fig. 8. The color of each point on the Hirshfeld surface corresponds to the relative contribution of that region to the overall molecular interactions, as defined by the pair of distance parameters (d_e, d_i). Points with smaller contributions to the surface are shown in blue, whereas those with the greatest contributions appear in red, while regions with no contribution remain uncolored. The d_{norm} parameter, derived from the normalized sum of d_i and d_e; the internal and external distances from the surface to the nearest atoms, respectively, provides a quantitative measure of contact distances relative to van der Waals separations. Accordingly, the mapped d_{norm} surfaces of DETCdBr (a) display more intense and widespread red regions compared to DETBr (b), highlighting the presence of shorter intermolecular contacts and stronger interactions. The red regions around the H···O and H···Br contact sites in DETCdBr reflect significant intermolecular interactions, consistent with the inclusion of the coordinated water molecule that enhances hydrogen-bonding connectivity. In contrast, DETBr shows fewer and less intense red areas, suggesting a relatively weaker supramolecular network dominated by H···Br and H···H interactions. The shape index and curvedness maps further

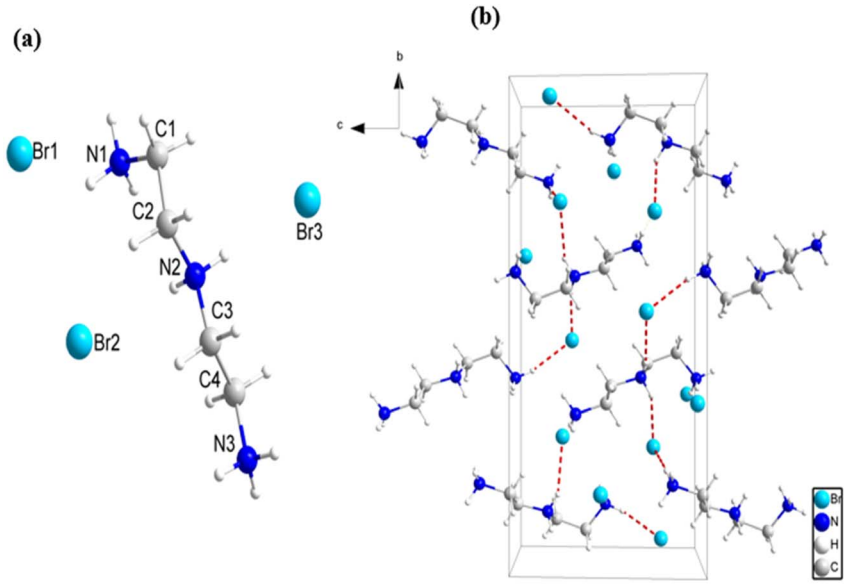

Fig. 7 (a) Asymmetric unit, (b) projection of the structure of DETBr on the (b and c) plane. The dotted lines indicate the hydrogen bonds.

illustrate the differences in molecular packing between the two crystals. DETCdBr shows more complex alternating red and blue patches on the shape index surface, highlighting complementary hollows and bumps that indicate close contact matching between neighbouring molecules. Its curvedness map also displays pronounced low-curvedness regions, reflecting flat surface areas associated with planar stacking and strong directional contacts. By contrast, DETBr presents smoother, less intricate patterns on both maps, implying a simpler packing arrangement governed mainly by van der Waals interactions.

The corresponding 2D fingerprint plots support these observations. For DETCdBr, the H···Br interactions contribute 69.1%, followed by H···H (24.2%) and H···O (6.4%), confirming the predominance of halogen- and hydrogen-bond interactions in the cadmium complex. Conversely, DETBr exhibits two main contributions: H···Br (66.4%) and H···H (33.5%), with no

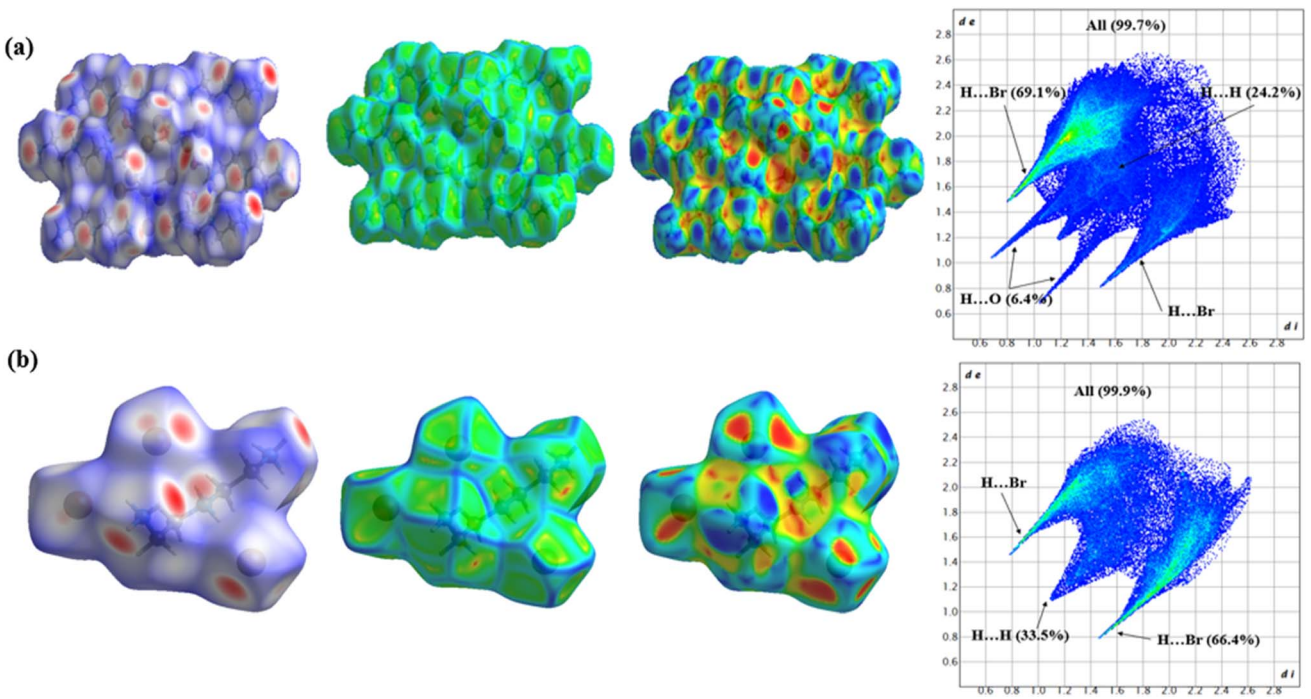

Fig. 8 Hirshfeld surfaces and 2D fingerprint plots for DETCdBr (a) and DETBr (b). For each compound, the Hirshfeld surface is shown mapped with d_{norm} (left), curvedness (center), and shape index (right).

detectable H···O contacts due to the absence of water molecules in its structure. These findings clearly indicate that coordination to Cd^{2+} and the incorporation of H_2O in DETCdBr strengthen the intermolecular contacts and result in a more compact and interconnected packing arrangement compared to the simpler organic salt DETBr.

3.4. Infrared spectroscopy investigations

FTIR spectroscopy was employed to confirm the presence and coordination of the organic components in both DETCdBr and the organic salt DETBr (Fig. 9). The assignment of the main absorption bands was established by comparison with previously reported data for similar hybrid materials.[7,8,51] A key difference is observed in the high-frequency region; DETCdBr exhibits a distinct broad band at 3462 cm^{-1}, attributed to ν(O–H) stretching vibrations, which confirms the presence of lattice water molecules within its hybrid structure, a feature absent in the precursor DETBr.

Both spectra show broad bands in the region from 3066 to 2339 cm^{-1}, attributed to N–H and C–H stretching modes. However, the pronounced broadening of the N–H bands in the DETCdBr compound suggests stronger hydrogen bonding interactions, consistent with the coordination of amine groups to the metal center and the presence of water molecules. Furthermore, the bands in the region of 1629–1581 cm^{-1} and at 1537 cm^{-1}, assigned to the asymmetric and symmetric bending vibrations $\delta(NH_3)$, respectively, show noticeable shifts and intensity changes in DETCdBr compared to DETBr. The wagging and twisting modes of NH_2 and CH_2 groups appear in the 1392–1477 cm^{-1} range for both compounds. Finally, the region below 1095 cm^{-1}, corresponding to C–C, C–N, C–N–C, and C–C–N skeletal vibrations, also shows clear modifications upon metal complexation. These comparative observations confirm the successful integration of the organic cation into the inorganic framework in DETCdBr.

3.5. Optical properties

3.5.1. Optical absorption and fundamental gap energy. The electronic transitions within the two structures were investigated through an analysis of the solid-state optical absorption properties of both compounds. Diffuse reflectance spectra were collected and converted into absorption spectra using the Kubelka–Munk (K–M) function,[54]

$$F(R) = (1 - R)^2/2R$$

where R is the reflectance and $F(R)$ is the K–M absorption.

The UV-visible absorption spectra of the two compounds, DETCdBr and DETBr, reveal a clear contrast in their optical responses (Fig. 10). The organic salt DETBr (**2**) displays a single intense absorption band in the deep-UV region; 200–220 nm, which can be attributed to localized n → σ* transitions involving the nitrogen lone pairs of the ammonium and amine groups. Such transitions are characteristic of non-conjugated organic systems and occur at high energies due to the absence of π-delocalized orbitals or charge-transfer processes. In contrast, the cadmium-based compound $(C_4H_{16}N_3)[CdBr_5]\cdot H_2O$ exhibits a much richer and broader absorption profile extending from the UV to the visible region. The intense bands observed around 250–320 nm and 360–420 nm can be assigned to halide-to-metal charge-transfer (LMCT) transitions and to electronic excitations arising from orbital overlap within the $[CdBr_5]$ coordination units. The broad tail extending into the visible region reflects the presence of low-energy charge-transfer or excitonic states introduced by the metal–halide framework and the structural heterogeneity of the inorganic sublattice, including variations in bromine coordination and interactions with lattice water molecules.

These spectral features clearly demonstrate that the incorporation of Cd^{2+} ions profoundly modifies the electronic structure, creating new intermediate states at lower energy compared to the purely organic phase. Consistently, the optical band gaps (E_g) determined from Tauc plots confirm this trend

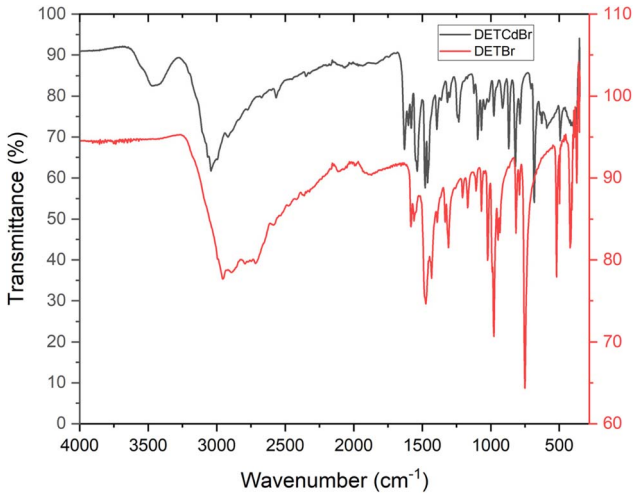

Fig. 9 FT-IR spectra of DETCdBr and DETBr the 400–4000 cm^{-1} region.

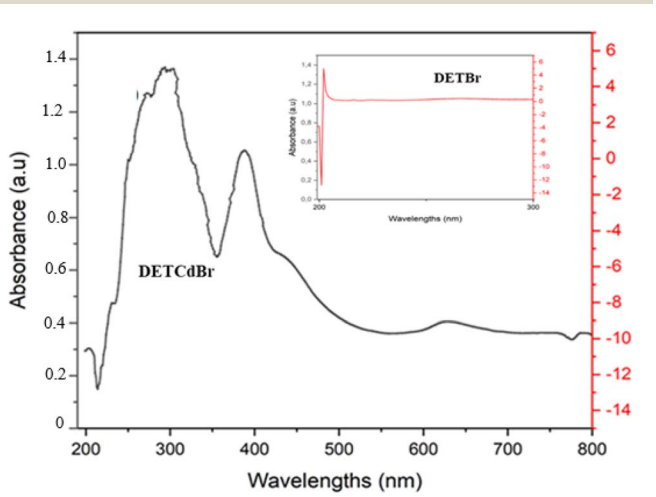

Fig. 10 Absorption spectra of DETCdBr (black trace) and DETBr (red trace).

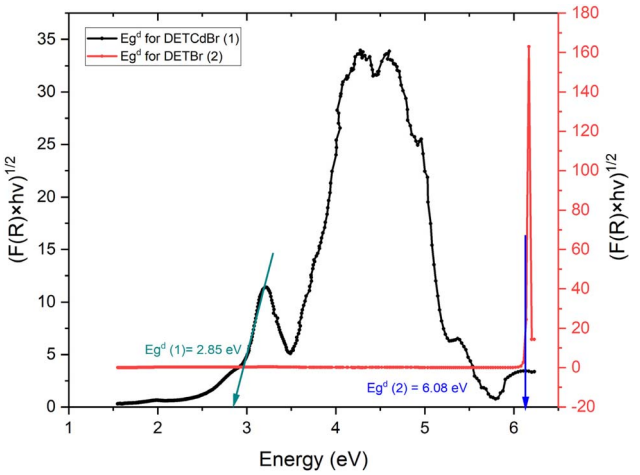

Fig. 11 Optical band gap determination of DETCdBr and DETBr.

in Fig. 11. The compound DETCdBr exhibits a direct band gap of approximately 2.85 eV, indicative of semiconducting behavior, whereas DETBr presents a much wider gap of about 6.08 eV, typical of insulating materials. The significant reduction in E_g upon cadmium coordination highlights the key role of metal–halide interactions, which enhance orbital overlap and facilitate charge delocalization, effectively lowering the transition energy.[55] Such electronic tuning is well-documented in hybrid metal–halide frameworks[56] and provides a promising pathway for designing materials with tailored optical and optoelectronic properties.[57]

3.5.2. Photoluminescence properties: white light emission. Fig. 12a presents the excitation-wavelength-dependent photoluminescence spectra recorded in the 300–500 nm range. A pronounced dependence of the emission intensity on the excitation wavelength is observed, whereas the overall spectral shape remains nearly unchanged. Under shorter-wavelength excitation, the compound displays a strong PL response, particularly in the high-energy region below 400 nm. As the excitation wavelength is increased, a gradual decrease in the PL intensity is observed across the entire emission window. In contrast, the broad emission band spanning approximately 450–650 nm preserves its position, showing no detectable spectral shift, with only a moderate attenuation in intensity. This behavior indicates that the emission originates from the same emissive states for all excitation energies, and that the excitation wavelength primarily affects the excitation efficiency rather than introducing new radiative recombination pathways.

Fig. 12b displays the CIE 1931 chromaticity diagram corresponding to the emission of DETCdBr compound. The chromaticity coordinates of the emitted light are located at approximately (0.32, 0.34), placing the emission point in the white-light region, close to the equi-energy point of standard daylight.[58] This position indicates a balanced contribution of the different emission components, resulting in a near-neutral white appearance. The proximity of these coordinates to the reference white point confirms the ability of the compound to generate white light, making it a promising candidate for solid-state lighting applications.

Fig. 12c presents the CIE 1931 chromaticity diagram corresponding to the emission of the organic salt $(C_4H_{16}N_3)Br_3$ (DETBr). The chromaticity coordinates are located at approximately (0.30, 0.32), which also fall within the white-light region, although slightly shifted from the ideal equi-energy white point. This position suggests that the emitted light retains a quasi-balanced spectral distribution, but with a minor deviation that may be associated with a slight dominance of specific emission components. Compared to DETCdBr, this small shift reflects differences in the emission origin, as DETBr emission is primarily governed by the organic moiety rather than inorganic coordination units. Nevertheless, the coordinates remain close enough to the reference white point to confirm that DETBr is also capable of producing near-white light, further supporting its potential in light-emitting applications.

3.6. *In silico* study

3.6.1. DFT and energy analysis of DETBr and DETCdBr. The electronic structure of DETBr and DETCdBr was investigated using density of states (DOS) and frontier molecular orbital (FMO) analysis, and global reactivity descriptors, as shown in (Fig. 13 and 14). DETBr exhibits HOMO and LUMO energies of −22.03 eV and −13.65 eV, respectively, with a wide energy gap of 8.378 eV, while DETCdBr shows HOMO and LUMO energies of −17.018 eV and −13.714 eV, resulting in a reduced gap of 3.304 eV. This significant decrease indicates enhanced electronic delocalization upon Cd coordination.

The optical band gaps follow the same trend, where DETBr displays an insulating character (~6.08 eV), whereas DETCdBr exhibits semiconducting behavior (~2.85 eV), confirming good agreement between theoretical and experimental results. FMO analysis reveals a clear spatial separation between HOMO (localized on electron-rich ligand regions) and LUMO (distributed over the π-system), suggesting intramolecular charge-transfer character, which is more pronounced in DETCdBr.

Global reactivity descriptors further support these findings, where DETCdBr shows lower chemical hardness ($\eta = 1.65$ eV) and higher softness ($S = 0.605$ eV^{-1}) compared to DETBr ($\eta = 4.19$ eV, $S = 0.239$ eV^{-1}). Additionally, the higher electrophilicity index of DETCdBr ($\omega \approx 71.5$ eV) indicates stronger electron-accepting ability and enhanced reactivity (Table S5). Overall, Cd coordination effectively turns the electronic structure from a wide-gap insulating system (DETBr) to a narrower-gap semiconducting system (DETCdBr) with improved charge-transfer properties.

3.6.2. Estimation of biological availability. The molecular behavior of DETBr and DETCdBr in biological systems was evaluated by predicting their key physicochemical and pharmacokinetic properties using SwissADME (Table S6 and Fig. 15). DETBr exhibited a molecular weight (MW) of 345.93 g mol^{-1} and a topological polar surface area (TPSA) of 71.89 Å^2, reflecting ideal drug-like dimensions, whereas the hybrid cadmium complex DETCdBr displayed considerably higher values (MW 636.16 g mol^{-1}, TPSA 162.24 Å^2) due to its bulky

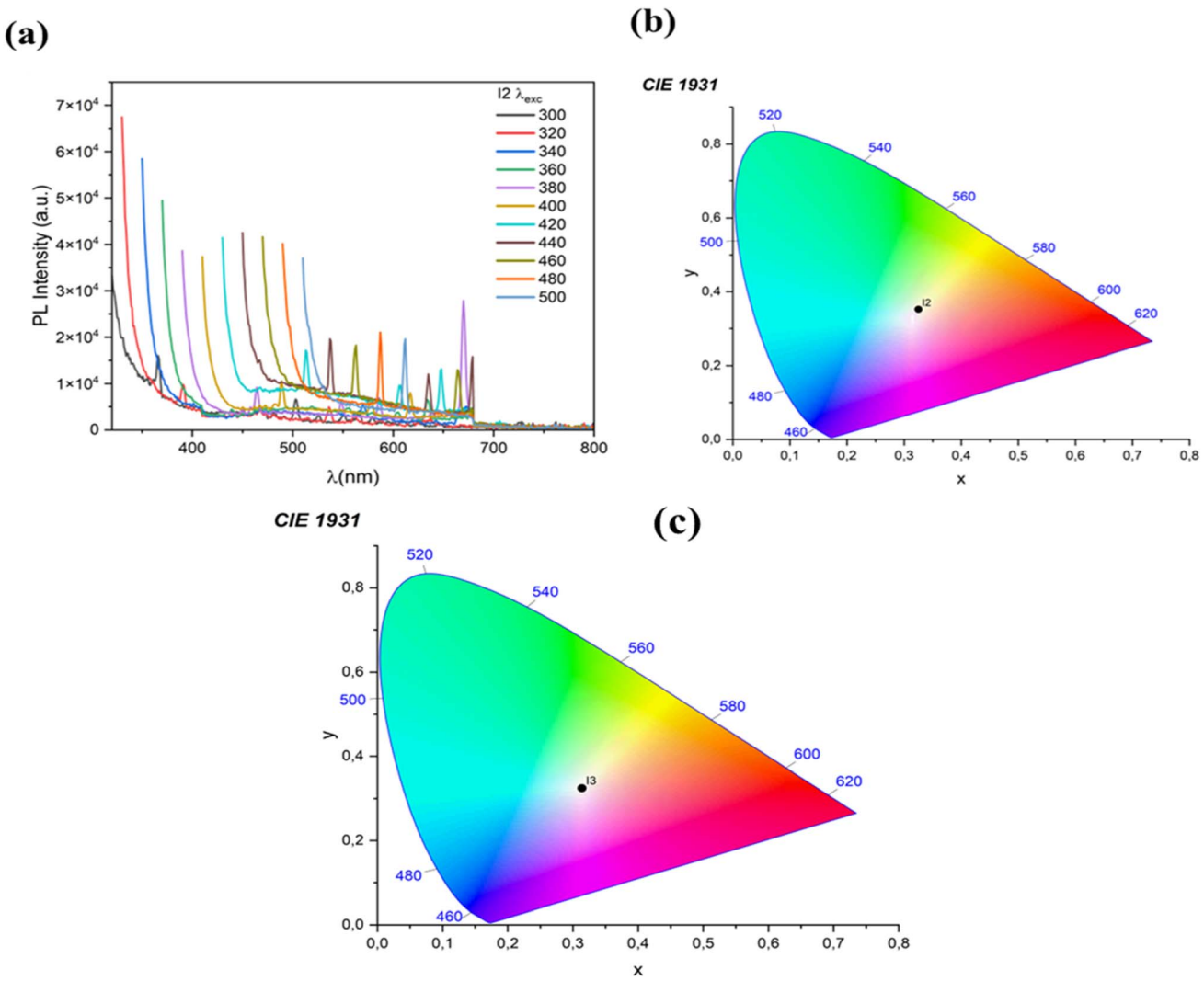

Fig. 12 Excitation wavelength dependence of PL spectra of DETCdBr (a) CIE coordinates of the DETCdBr (b) CIE coordinates of the DETBr (c).

binuclear cadmium framework. Both compounds are highly hydrophilic, with consensus log P values of −4.75 and −10.58, favoring interactions with the polar residues of the α-amylase active site. DETBr showed superior water solubility (Ali log S = −1.92) and full compliance with Lipinski's and Veber's rules, yielding a high bioavailability score (0.55). The pharmacokinetic profile predicted low gastrointestinal (GI) absorption and no blood–brain barrier (BBB) permeation for both molecules, a desirable feature for localized intestinal enzyme inhibition while minimizing systemic toxicity. Additionally, the low synthetic accessibility (SA) score for DETBr (1.42) indicates ease of synthesis compared to the more complex coordination environment of DETCdBr (4.17).

3.6.3. Molecular docking with α-amylase (PDB ID: 4W93). Docking studies evaluated the interactions of DETBr and DETCdBr with human pancreatic α-amylase (Table S7 and Fig. 16, 17). The reference inhibitor, acarbose, exhibited the highest binding affinity (−8.32 kcal mol^{-1}), stabilized by hydrogen bonds with Asp300, Thr163, and Gln63, and H–π interactions with Trp59, consistent with its known inhibitory mechanism.

DETBr, modeled as the tri-protonated diethylenetriammonium, showed a binding affinity of −4.84 kcal mol^{-1}. Its inhibition is mainly driven by hydrogen bonds and electrostatic interactions between the terminal –NH_3^+ groups and the catalytic residues Asp197 and Asp300, effectively neutralizing the catalytic nucleophiles and impeding starch hydrolysis.

The hybrid cadmium complex DETCdBr exhibited a slightly stronger binding affinity (−5.43 kcal mol^{-1}), with additional stabilization from bromide-mediated hydrogen-acceptor and ionic contacts involving His305 and Asn298. While the cadmium cluster serves as a structural scaffold orienting the bioactive cations, its bulk imposes steric limitations, preventing full access of the pharmacophore to the catalytic pocket.

Overall, both DETBr and DETCdBr target key catalytic residues, confirming their potential as α-amylase inhibitors. DETBr offers a more drug-like profile with lower molecular weight and higher solubility, whereas DETCdBr benefits from enhanced

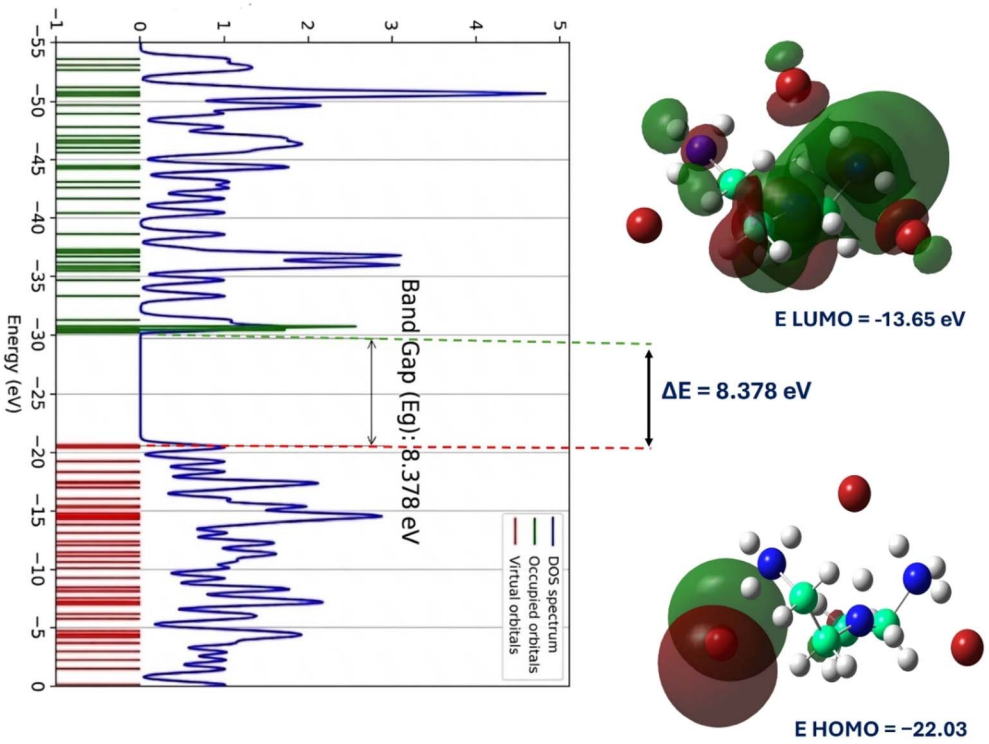

Fig. 13 The DOS spectrum for DETBr.

binding orientation due to the inorganic framework. These findings highlight the importance of molecular composition in optimizing enzyme inhibition, suggesting selective intestinal activity with minimal systemic absorption.[52,53]

3.7. Biological activities

3.7.1. Substrate-dependent enzymatic activity and inhibitory effect of DETBr and DETCdBr. Fig. 18 illustrates how

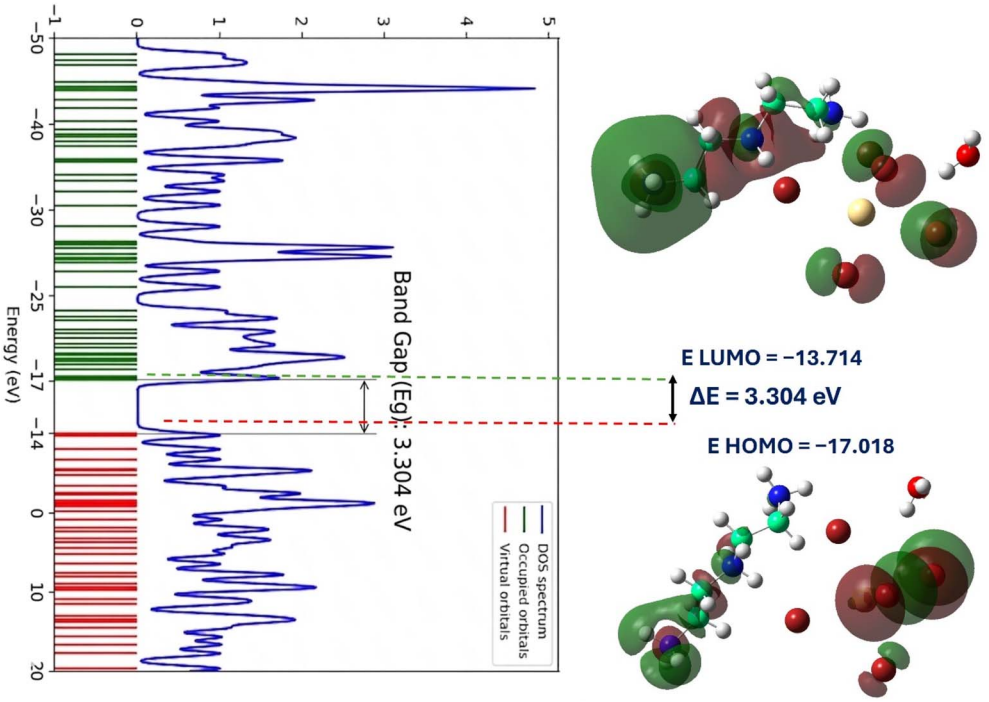

Fig. 14 The DOS spectrum for DETCdBr.

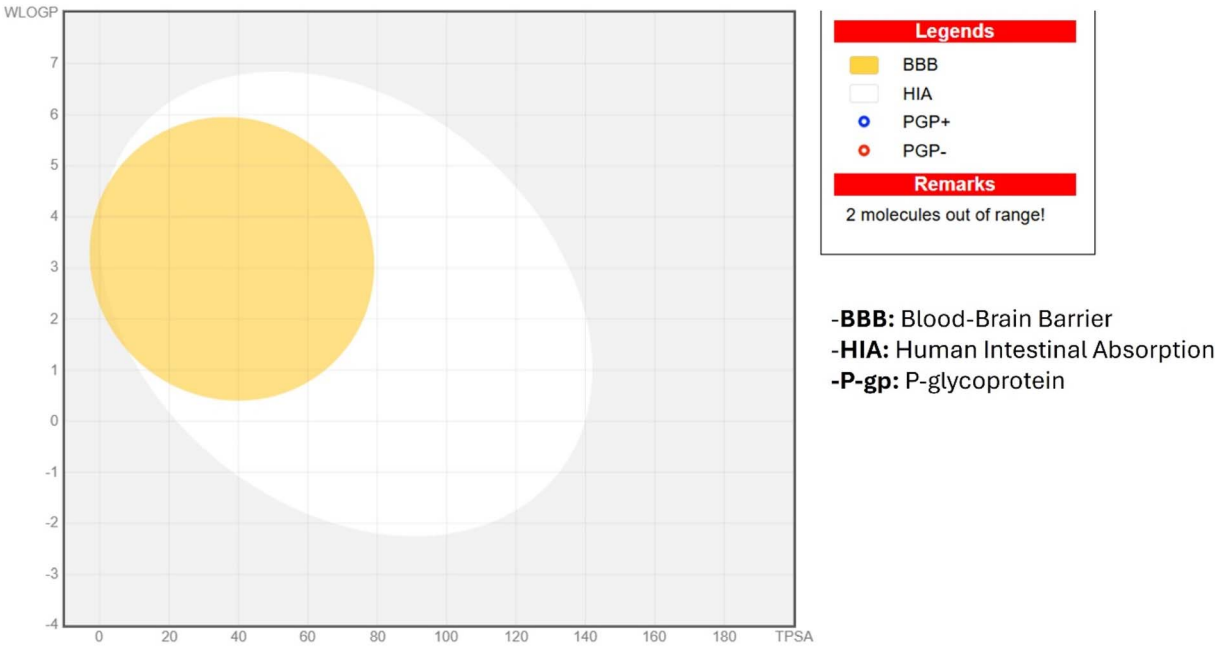

Fig. 15 BOILED-Egg model predictions for DETBr and DETCdBr.

increasing starch concentration affects α-amylase activity both without and with DETBr and DETCdBr. In the control, enzyme activity rises quickly with substrate concentration, following typical Michaelis–Menten kinetics. Conversely, both compounds significantly decrease α-amylase activity across all tested concentrations, although the reaction rate still increases with substrate concentration, indicating that the inhibition can be partially overcome by excess substrate behavior typical of competitive inhibition. Notably, DETBr shows a stronger inhibitory effect than DETCdBr. Their structural features explain this difference: DETBr consists of discrete ionic units of triprotonated diethylenetriamine and bromide ions, offering a more accessible and flexible structure that may interact more effectively with the enzyme. In contrast, DETCdBr forms a compact hybrid inorganic–organic framework made of one-dimensional $[CdBr_5]_n^{3-}$ chains stabilized by extensive hydrogen bonds, which could limit access to active functional groups for the enzyme. Overall, these results suggest that the molecular organization of these compounds plays an important role in modifying their inhibitory activity toward α-amylase.

3.7.2. Concentration-dependent inhibition behavior of DETBr and DETCdBr compared to acarbose. DETBr has a unique inhibitory profile against α-amylase compared to acarbose (Fig. 19a). DETBr demonstrated strong inhibition at the lowest tested concentration (about 70% at 0.25 mg mL^{-1}), then gradually decreased as the concentration increased, indicating

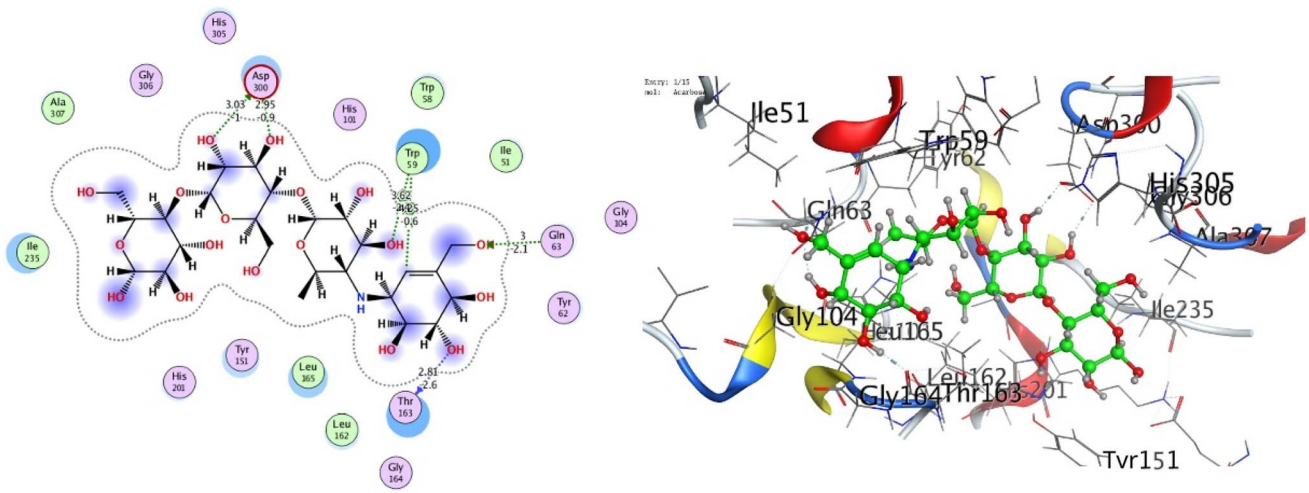

Fig. 16 2D, 3D for molecular docking of acarbose with α-amylase.

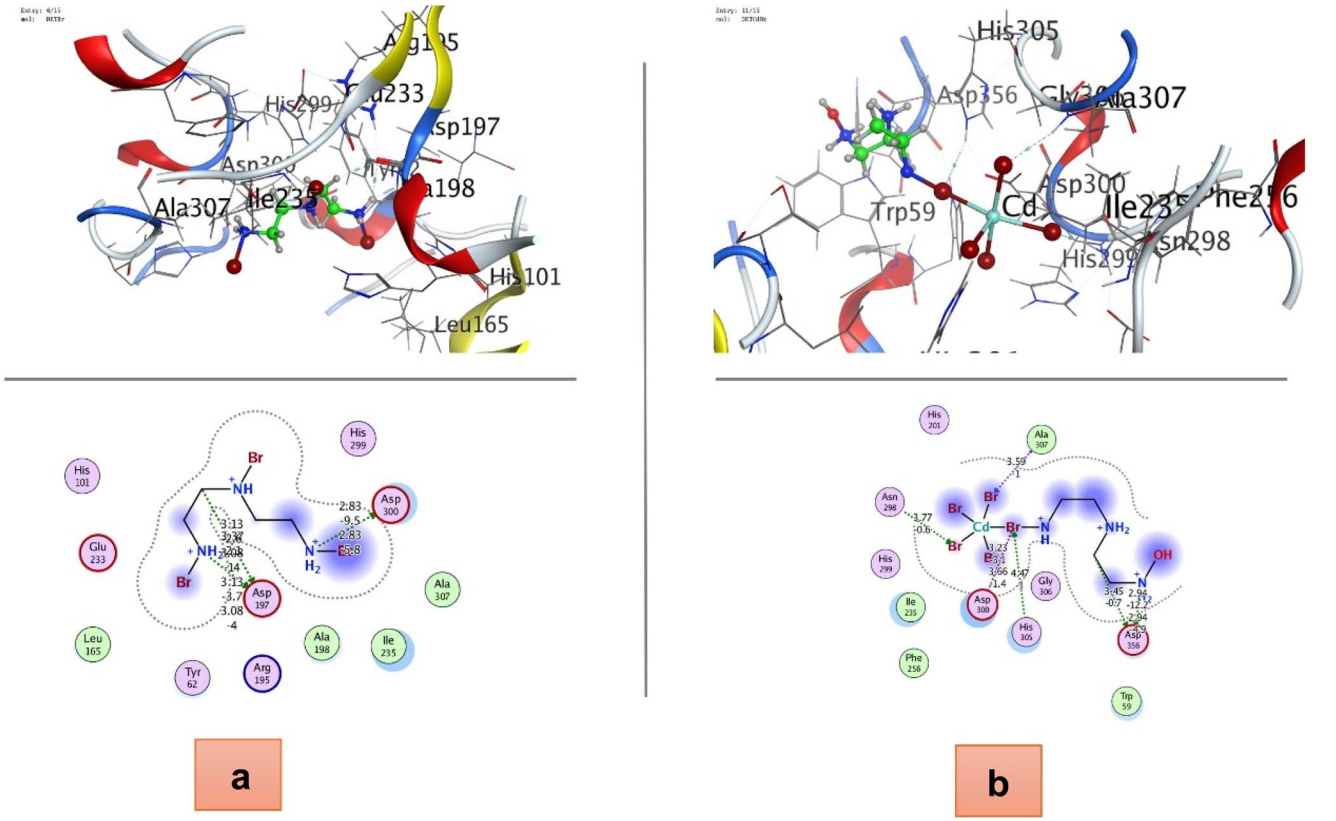

Fig. 17 2D, 3D for molecular docking of (a) DETBr, and (b) DETCdBr with α-amylase (PDB ID: 4W93).

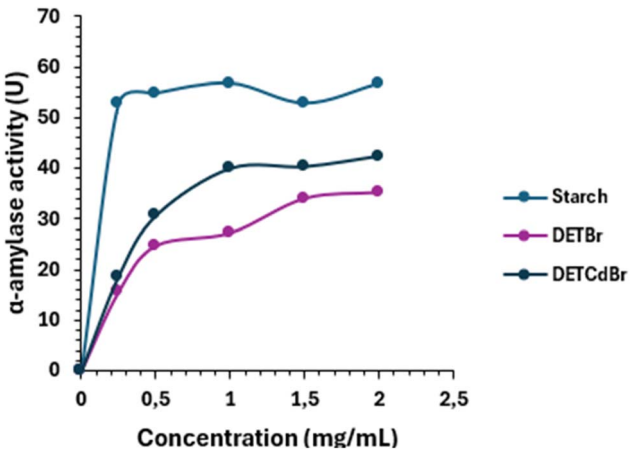

Fig. 18 Evolution of α-amylase enzymatic activity in the presence and absence of DETBr and DETCdBr.

a non-traditional dose–response pattern. In contrast, acarbose exhibited a typical concentration-dependent inhibition, increasing steadily to nearly 80% at 2 mg mL^{-1}, consistent with its well-known role as a competitive α-amylase inhibitor.

This unusual inhibitory behavior of DETBr can be explained by its structural features. Crystallographic analysis showed that DETBr consists of distinct ionic units formed by triprotonated diethylenetriamine cations and bromide anions, stabilized by N–H···Br hydrogen bonds. The multiple protonated amine groups create positively charged sites capable of interacting with negatively charged residues near the catalytic region of α-amylase, especially Asp197, Glu233, and Asp300, which are involved in substrate binding and catalysis. These electrostatic and hydrogen-bonding interactions likely account for the strong inhibition observed at low concentrations.

SEM observations showing small, relatively porous particles, along with Hirshfeld surface analysis highlighting the dominance of N–H···Br interactions, further suggest that the molecular organization of DETBr promotes surface accessibility and enzyme interactions. However, the decrease in inhibition at higher concentrations might be due to intermolecular associations or partial aggregation in solution, which can reduce the availability of active protonated sites. Overall, these findings emphasize a clear structure–activity relationship, indicating that the accessibility of protonated amine groups in DETBr plays a crucial role in modulating its α-amylase inhibitory activity.

In the other hand, Fig. 19b illustrates the inhibitory activity of DETCdBr against α-amylase in comparison to acarbose. DETCdBr showed the highest inhibition at the lowest concentration (around 65% at 0.25 mg mL^{-1}), with a gradual decrease as the concentration increased, indicating a negative concentration–response trend. Conversely, acarbose demonstrated a typical dose-dependent inhibition, rising steadily to nearly 80% at 2 mg mL^{-1}. Although DETCdBr is more effective than acarbose at very low concentrations, its inhibitory ability

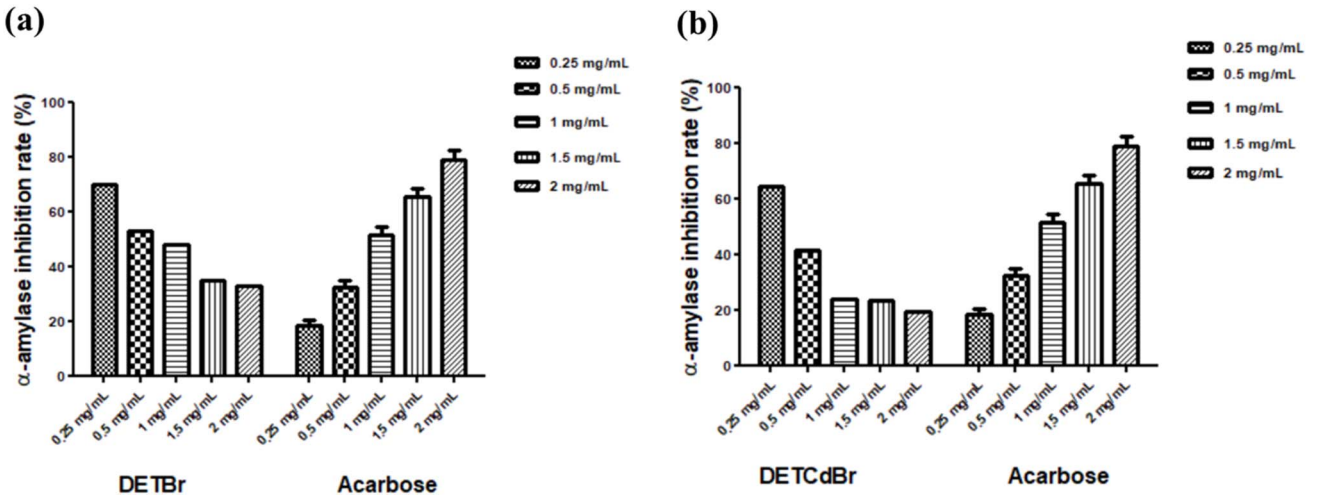

Fig. 19 α-Amylase inhibition rate of DETBr and acarbose (a) DETCdBr and acarbose (b).

diminishes at higher doses, suggesting reduced access to the enzyme's active site or possible molecular aggregation.

The structural features of DETCdBr explain these results. Crystallographic analysis showed a one-dimensional hybrid inorganic–organic framework made of $[CdBr_5]_n^{3-}$ chains connected through hydrogen bonds with triprotonated diethylenetriamine cations and water molecules in the lattice. The rigid, tightly packed supramolecular structure, supported by SEM and Hirshfeld surface analyses, may reduce the availability of functional amine groups for interaction with the catalytic residues of α-amylase (Asp197, Glu233, and Asp300), which explains the decrease in inhibition at higher concentrations.

Overall, the biological activity of DETCdBr reflects a clear structure–function relationship: while the accessible protonated amine groups enable significant inhibition at low concentrations, the compact hybrid framework limits enzyme interactions at higher doses, unlike the flexible and more accessible structure of DETBr or the substrate-mimicking structure of acarbose.

3.7.3. Kinetic analysis of α-amylase inhibition by DETBr (competitive mechanism) and DETCdBr (non-competitive mechanism). Fig. 20 shows Lineweaver–Burk plots used to examine how DETBr inhibits α-amylase. The lines intersect near the *y*-axis, indicating that V_{max} remains unchanged, while the apparent K_m increases from 1.25 mg mL^{-1} (starch alone) to 5 mg mL^{-1} in the presence of DETBr, supporting a competitive inhibition mechanism. The estimated inhibition constant (K_i = 0.33 mg mL^{-1}) suggests a moderate binding affinity of DETBr for the enzyme's active site. This behavior can be explained by the structural features of DETBr, which consists of discrete ionic units of triprotonated diethylenetriamine cations and bromide anions stabilized by N–H···Br hydrogen bonds. The positively charged amine groups can interact with negatively charged residues in the catalytic site of α-amylase (Asp197, Glu233, and Asp300), effectively competing with the substrate without affecting the catalytic turnover. SEM and Hirshfeld analyses further support this by revealing a morphology and hydrogen-bonding network that favor such interactions. In

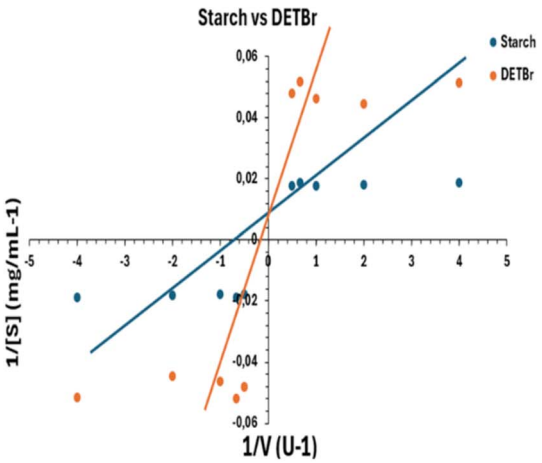

Competitive inhibitor

	Km (mg/mL)	Vmax (U)	[I] (mg/mL)	Ki (mg/mL)
Starch	1,25	125	1	0,33
DETBr	5			

- Vmax (maximum velocity)
- Km (Michaelis–Menten constant)
- Ki (inhibition constant)
- [I] (inhibitor concentration)

$$k_i = \frac{[I]}{\left(\frac{KM}{KMapp} - 1\right)}$$

Fig. 20 Lineweaver–Burk plots of α-amylase inhibition at different substrate (starch) concentrations in the presence of DETBr.

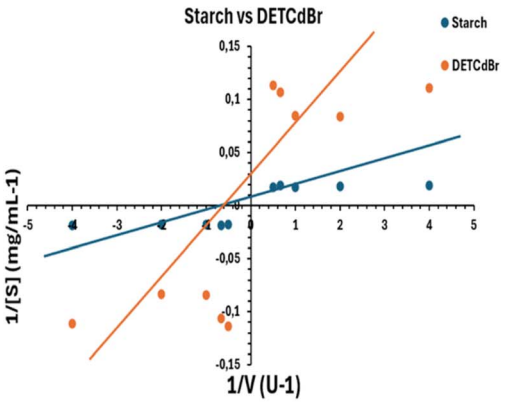

Non-competitive inhibitor

	Km (mg/mL)	Vmax (U)	[I] (mg/mL)	Ki (mg/mL)
Starch	1,67	100	0,5	0,25
Detcd Br		33,33		

- Vmax (maximum velocity)
- Km (Michaelis–Menten constant)
- Ki (inhibition constant)
- [I] (inhibitor concentration)

$$k_i = \frac{[I]}{\left(\frac{v_{max}}{v_{max\,app}} - 1\right)}$$

Fig. 21 Lineweaver–Burk plots of α-amylase inhibition at different substrate (starch) concentrations in the presence of DETCdBr.

contrast, Fig. 5 presents the kinetic behavior of DETCdBr, where the Lineweaver–Burk plots intersect on the *x*-axis, indicating that K_m remains constant at 1.67 mg mL^{-1} while V_{max} decreases from 100 to 33.33 U, characteristic of a non-competitive inhibition mechanism. The corresponding inhibition constant (K_i = 0.25 mg mL^{-1}) reflects a moderate interaction with the enzyme.

Unlike DETBr, DETCdBr does not affect substrate binding but reduces catalytic efficiency, likely due to conformational changes induced upon binding, as shown in Fig. 21. The kinetic behavior of DETCdBr toward α-amylase was studied using Lineweaver–Burk double-reciprocal plots. In the presence of DETCdBr, the plots intersect on the *x*-axis, indicating that the Michaelis constant (K_m) remains unchanged at 1.67 mg mL^{-1}, while the maximum reaction velocity (V_{max}) decreases from 100 to 33.33 U. This pattern is typical of non-competitive inhibition, where the inhibitor binds to an allosteric site separate from the catalytic center and can interact with both the free enzyme and the enzyme–substrate complex.

The inhibition constant calculated from the reduction in V_{max} was K_i = 0.25 mg mL^{-1}, indicating a moderate yet significant interaction between DETCdBr and α-amylase. The preservation of K_m suggests that substrate binding to the catalytic pocket remains unaffected, while the decrease in V_{max} reflects a reduction in catalytic turnover, likely caused by conformational changes induced by inhibitor binding.

From a structural standpoint, this inhibitory behavior may relate to the rigid supramolecular architecture of DETCdBr, which consists of $[Cd_2Br_{10}]^{6-}$ dimeric units stabilized by hydrogen bonds with triprotonated diethylenetriamine cations and lattice water molecules. This extended hybrid framework might restrict direct entry into the enzyme's active site while promoting interactions with peripheral or regulatory regions of the enzyme. Such interactions can cause structural changes that modify enzymatic activity without disrupting substrate recognition. Interestingly, this mode of inhibition differs from the behavior observed for DETBr, which functions as a competitive inhibitor. The difference likely stems from structural flexibility: DETBr has more accessible protonated amine groups that can directly interact with the catalytic pocket, whereas the more rigid, sterically hindered structure of DETCdBr promotes allosteric interactions. Taken together, these observations highlight a clear structure–function relationship, where the molecular organization and accessibility of functional groups govern the inhibition mechanism and efficiency of bromide-based diethylenetriamine derivatives toward α-amylase.

4 Conclusion

Two new diethylenetriamine-derived bromide compounds were successfully synthesized and characterized: the hybrid inorganic–organic material $(C_4H_{16}N_3)[CdBr_5]\cdot H_2O$ (DETCdBr) and the organic salt $(C_4H_{16}N_3)Br_3$ (DETBr). Single-crystal X-ray diffraction shows that both crystallize in the monoclinic system ($P2_1/c$) but exhibit distinct structural organizations. DETCdBr is built from dimeric $[Cd_2Br_{10}]^{6-}$ units forming hydrogen-bonded networks, whereas DETBr consists of discrete ions stabilized by N–H···Br interactions. Phase purity and morphology analyses confirm a more compact and cohesive structure for DETCdBr compared to the more porous DETBr, in agreement with Hirshfeld surface results highlighting stronger intermolecular interactions in the hybrid compound. Optical measurements reveal a marked contrast between the two systems: DETBr behaves as a wide-band-gap material with deep-UV absorption, while DETCdBr exhibits a reduced band gap (~2.85 eV) and extended absorption into the visible region, characteristic of charge-transfer transitions. Both compounds display near white-light emission, supporting their potential in solid-state lighting applications. *In silico* investigations corroborate these findings, showing enhanced electronic delocalization and reactivity for DETCdBr, while DETBr exhibits more favorable drug-like properties. Molecular docking and biological assays demonstrate that both compounds inhibit α-amylase through distinct mechanisms: competitive for DETBr and non-competitive for DETCdBr. Overall, these results highlight the key role of metal coordination in tuning structural, optical, and biological properties, offering a rational strategy for designing multifunctional hybrid materials.

Author contributions

Iteb Ben Mahmoud: formal analysis, writing-original draft; Mashael A. Alghamdi: data curation, investigation; Houda Lazreg Aref: data curation, validation; Noureddine Mhadhbi: conceptualization, data analysis; Hossam H. Nasrallah: formal analysis, investigation; Ahlem Guesmi: validation, software; Naoufel Ben Hamadi: investigation, formal analysis; Sandra Walha: methodology, investigation; Ferdinando Costantino: formal analysis, investigation; Houcine Naïli: project administration, review & editing.

Conflicts of interest

The authors declare that they have no known competing financial interests or personal relationships that could have appeared to influence the work reported in this paper.

Data availability

The data that supported the findings of this study are available upon reasonable request.

CCDC 2543017 (DETBr) and 2543018 (DETCdBr) contain the supplementary crystallographic data for this paper.[59a,b]

Supplementary information (SI): crystallographic, structural, computational, ADME, and molecular docking data. See DOI: https://doi.org/10.1039/d6ra02827f.

Funding

This work was supported and funded by the Deanship of Scientific Research at Imam Mohammad Ibn Saud Islamic University (IMSIU) (grant number IMSIU-DDRSP2603).

References

1 M. Abid, M. M. Turnbull, H. Naïli and W. Rekik, A new mixed halide 2D hybrid perovskite : Structural , thermal , optic and magnetic properties, *Polyhedron*, 2020, **175**, 114220, DOI: 10.1016/j.poly.2019.114220.

2 N. Mhadhbi, S. Saïd, S. Elleuch, T. Lis and H. Naïli, Experimental and DFT characterization of the organic–inorganic monohydrated Co(II) complex with 2,6-diaminopyridine ligand, (C5H8N3)2[CoBr4]·H2O, *J. Mol. Struct.*, 2016, **1105**, 16–24, DOI: 10.1016/j.molstruc.2015.10.025.

3 H. Tlili, S. Walha, S. Elleuch, B. Fares and H. Naïli, Structural, vibrational, DFT and optical studies of a new non-centrosymmetric hybrid material (C4H12N2)[CoBr4], *J. Mol. Struct.*, 2018, **1152**, 303–310, DOI: 10.1016/j.molstruc.2017.09.096.

4 N. L. Nkhili, W. Rekik, T. Mhiri, K. T. Mahmudov, M. N. Kopylovich and H. Naïli, Double piperazinediium and 1,4-diazabicyclo[2.2.2]octanediium M II selenates (M II = Co II , Ni II , Cu II , Zn II) as effective catalysts for Henry reaction, *Inorg. Chim. Acta*, 2014, **412**, 27–31, DOI: 10.1016/j.ica.2013.12.007.

5 W. Rekik, H. Naïli, T. Mhiri and T. Bataille, A new dabco templated metal sulfate, (C6H14N2)[Mn(H2O)6](SO4)2. Chemical preparation, hydrogen-bonded structure and thermal decomposition, *J. Chem. Crystallogr.*, 2007, **37**, DOI: 10.1007/s10870-006-9170-9.

6 A. Maatar, B. Salah, N. Sayari, H. Naïli and A. J. Norquist, Chiral and achiral copper(II) complexes: structure, bonding and biological activities, *RSC Adv.*, 2016, 59055–59065, DOI: 10.1039/c6ra09630a.

7 N. Mhadhbi, R. Msalmi, E. Mosconi, J. Erwannd, H. Khmissi, M. Orendac, E. Cizmar and H. Naïli, Investigation of the electronic, optical and magnetic properties of a novel two-dimensional lead-free perovskite : High visible-light absorption and long-range magnetic ordering, *J. Alloys Compd.*, 2024, 1007, DOI: 10.1016/j.jallcom.2024.176450.

8 F. A. Saleemh, S. Musameh, A. Sawafta, P. Brandao, C. J. Tavares, S. Ferdov, A. Barakat, A. Al Ali, M. Al-noaimi and I. Warad, Diethylenetriamine/diamines/copper (II) complexes [Cu(dien)(NN)]Br2: Synthesis, solvatochromism, thermal, electrochemistry, single crystal, Hirshfeld surface analysis and antibacterial activity, *Arabian J. Chem.*, 2016, **10**, 845–854, DOI: 10.1016/j.arabjc.2016.10.008.

9 S. Walha, N. Mhadhbi, B. F. Ali, A. Kaiba, A. Guesmi, W. A. El-Fattah, N. Ben Hamadi, M. M. Turnbull, F. Costantino and H. Naïli, Hydrothermal synthesis of (C5H14N2)[CoCl4]□0.5H2O: Crystal structure, spectroscopic characterization, thermal behavior, magnetic properties and biological evaluation, *Chem. Phys. Impact*, 2024, **8**, 100597, DOI: 10.1016/j.chphi.2024.100597.

10 N. Olivi-Tran, A. Ferchichi, S. Calas and P. Etienne, Total electronic energy by tight binding approximation and experimental toughness of three different hybrid polymers, *J. Non-Cryst. Solids*, 2010, **356**, 287–289, DOI: 10.1016/j.jnoncrysol.2009.12.009.

11 A. M. Ben Salah, L. B. Fendri, T. Bataille, R. P. Herrera and H. Naïli, Synthesis, structural determination and antimicrobial evaluation of two novel CoII and ZnII halogenometallates as efficient catalysts for the acetalization reaction of aldehydes, *Chem. Cent. J.*, 2018, **12**, 1–12, DOI: 10.1186/s13065-018-0393-6.

12 T. Sahoo, U. A. Anene, S. K. Nayak and S. P. Alpay, Electronic and optical properties of zinc based hybrid organic-inorganic compounds Electronic and optical properties of zinc based hybrid organic- inorganic compounds, *Mater. Res. Express*, 2020, **7**, 035701, DOI: 10.1088/2053-1591/ab7ac4.

13 I. Althagafi, M. Morad, A. Y. Al, Y. Hanadi and A. K. Aisha, Synthesis and characterization for new Zn (II) complexes and their optimizing fertilization performance in planting corn hybrid, *Chem. Pap.*, 2021, **75**, 2121–2133, DOI: 10.1007/s11696-020-01440-7.

14 S. Boufas, N. Mohamedi, P. Bénard-Rocherullé, P. Roussel and T. Roisnel, CdCl3− vs CdCl42− in Hybrid Materials, *Proced. Soc. Behav. Sci.*, 2015, **195**, 1639–1647, DOI: 10.1016/j.sbspro.2015.06.229.

15 S. Alzahrani, M. Morad, A. Bayazeed, M. M. Aljohani, F. Alkhatib, R. Shah, H. Katouah, H. M. Abumelha,

I. Althaga, R. Zaky and N. M. El-metwaly, Ball milling approach to prepare new Cd (II) and Zn (II) complexes ; characterization , crystal packing , cyclic voltammetry and MOE-docking agrees with biological assay, *J. Mol. Struct.*, 2020, **1218**, 128473, DOI: 10.1016/j.molstruc.2020.128473.

16 J. Jin, M. J. Jia, Y. C. Wang, J. H. Yu, Q. F. Yang and J. Q. Xu, Structural characterization of three organically modified Cd(II) compounds, *Inorg. Chem. Commun.*, 2011, **14**, 1681–1684, DOI: 10.1016/j.inoche.2011.07.006.

17 R. Al-Far and B. F. Ali, Three dimensional network polymeric structure of (4,4′-bipyridinium) [CdBr4] n: Supramolecular motifs and crystal supramolecularity, *J. Chem. Crystallogr.*, 2008, **38**, 289–293, DOI: 10.1007/s10870-007-9298-2.

18 Y. Baklouti, N. Chaari, H. Feki, N. Chniba-Boudjada and F. Zouari, Crystal structure, vibrational studies, optical properties and DFT calculations of 2-amino-5-diethylaminopentanium tetrachlorocadmate (II), *Spectrochim. Acta, Part A*, 2015, **136**, 397–404, DOI: 10.1016/j.saa.2014.09.049.

19 M. Pisačić, I. Kodrin, A. Trninic and M. M. Đaković, Two-Dimensional Anisotropic Flexibility of Mechanically Responsive Crystalline Cadmium(II) Coordination Polymers, *Chem. Mater.*, 2022, **34**, 5, DOI: 10.1021/acs.chemmater.2c00062.

20 C. Hu and U. Englert, Coordination polymers based on cadmium (II) pyridine complexes: synthesis, range of existence, and structure, *RSC Adv.*, 2002, **5**, 20–25, DOI: 10.1039/b110208g.

21 S.-S. Han, Z.-W. He, L. Li and S.-S. Chen, A Cd(II) Coordination Polymer Based on Mixed Ligands: Synthesis, Crystal Structure, and Properties, *Crystals*, 2019, **9**(12), 625, DOI: 10.3390/cryst9120625.

22 S. Lin, X. Li, Q. Cui and H. He, Synthesis, Characterizations and Luminescent Properties of Two Cadmium (II) Coordination Polymers Derived from Bis(Benzimidazole)-Based Ligands, *J. Inorg. Organomet. Polym. Mater.*, 2013, 771–778, DOI: 10.1007/s10904-013-9825-x.

23 R. Msalmi, S. Elleuch, B. Hamdi, R. Zouari and H. Na, Synthesis , DFT calculations , intermolecular interactions and third order nonlinear optical properties of new organoammonium, *J. Mol. Struct.*, 2020, **1222**, 128853, DOI: 10.1016/j.molstruc.2020.128853.

24 I. Hamdi, Y. Khan, F. Aouaini and H. Seo, A copper-based 2D hybrid perovskite solar absorber as a potential eco-friendly alternative to lead halide perovskites, *J. Mater. Chem. C*, 2022, 3738–3745, DOI: 10.1039/d1tc05047h.

25 Y. Wu, M. Lin, D. Liu, M. Liu and J. Qian, Two-dimensional Cd (II) coordination polymer encapsulated by Tb 3 + as a reversible luminescent, *RSC Adv.*, 2019, **9**(60), 34949–34957, DOI: 10.1039/c9ra06639j.

26 J. Chen, *CrystEngComm*, 2024, **26**, 431–438, DOI: 10.1039/d3ce01096a.

27 J. Janczak, Coordination properties of diethylenetriamine in relation to zinc phthalocyanine, *Polyhedron*, 2020, **178**, 114313, DOI: 10.1016/j.poly.2019.114313.

28 G. M. Sheldrick, SHELXT - Integrated space-group and crystal-structure determination, *Acta Crystallogr., Sect. A:Found. Crystallogr.*, 2015, **71**, 3–8, DOI: 10.1107/S2053273314026370.

29 O. V. Dolomanov, L. J. Bourhis, R. J. Gildea, J. A. K. Howard and H. Puschmann, OLEX2: a complete structure solution, refinement and analysis program, *J. Appl. Crystallogr.*, 2009, 339–341, DOI: 10.1107/S0021889808042726.

30 G. M. Sheldricka, Crystal structure refinement with SHELXL, *Struct. Chem.*, 2014, **71**, 3–8, DOI: 10.1107/S2053229614024218.

31 K. Brandenburg, *Diamond Version 3.2k, Diamond Version 4.4.2*, 2016, Bonn.

32 D. J. P. R. Spackman, M. J. Turner, J. J. McKinnon, S. K. Wolff, M. A. S. Grimwood and D. Jayatilaka, CrystalExplorer: a program for Hirshfeld surface analysis, visualization and qu-antitative analysis of molecular crystals, *J. Appl. Crystallogr.*, 2021, **54**, 1006–1011, DOI: 10.1107/S1600576721002910.

33 B. G. Janesko, Replacing hybrid density functional theory: motivation and recent advances, *Chem. Soc. Rev.*, 2021, **50**, 8470–8495, DOI: 10.1039/D0CS01074J.

34 A. M. Abbas, A. Aboelmagd, S. M. Kishk, H. H. Nasrallah, W. C. Boyd, H. Kalil and A. S. Orabi, A Novel Ibuprofen Derivative and Its Complexes: Physicochemical Characterization, DFT Modeling, Docking, In Vitro Anti-Inflammatory Studies, and DNA Interaction, *Molecules*, 2022, **27**(21), 7540, DOI: 10.3390/molecules27217540.

35 A. M. Abbas, H. H. Nasrallah, A. Aboelmagd, S. M. Kishk, W. C. Boyd, H. Kalil and A. S. Orabi, Design, Synthesis, Anti-Inflammatory Activity, DFT Modeling and Docking Study of New Ibuprofen Derivatives, *Int. J. Mol. Sci.*, 2024, **25**, 3558, DOI: 10.3390/ijms25063558.

36 A. Daina, O. Michielin and V. Zoete, SwissADME: a free web tool to evaluate pharmacokinetics, drug-likeness and medicinal chemistry friendliness of small molecules, *Sci. Rep.*, 2017, **7**, 42717, DOI: 10.1038/srep42717.

37 L. K. Williams, S. Caner and G. D. Brayer, *Human Pancreatic Alpha-Amylase in Complex with Montbretin A: 4w93*, 2015, DOI: 10.2210/pdb4w93/pdb.

38 L. K. Williams, X. Zhang, S. Caner, C. Tysoe, N. T. Nguyen, J. Wicki, D. E. Williams, J. Coleman, J. H. McNeill, V. Yuen, R. J. Andersen, S. G. Withers and G. D. Brayer, The amylase inhibitor montbretin A reveals a new glycosidase inhibition motif, *Nat. Chem. Biol.*, 2015, **11**, 691–696, DOI: 10.1038/nchembio.1865.

39 J. Eberhardt, D. Santos-Martins, A. F. Tillack and S. Forli, AutoDock Vina 1.2.0: New Docking Methods, Expanded Force Field, and Python Bindings, *J. Chem. Inf. Model.*, 2021, **61**, 3891–3898, DOI: 10.1021/acs.jcim.1c00203.

40 A. M. Abbas, H. Hossam, A. Aboelmagd, W. C. Boyd, H. Kalil and A. S. Orabi, Novel Trimethoprim-Based Metal Complexes and Nanoparticle Functionalization: Synthesis, Structural Analysis, and Anticancer Properties, *Inorganics*, 2025, **13**, 144, DOI: 10.3390/inorganics13050144.

41 O. Trott and A. J. Olson, AutoDock Vina: Improving the speed and accuracy of docking with a new scoring function, efficient optimization, and multithreading, *J. Comput. Chem.*, 2010, **31**, 455–461, DOI: 10.1002/jcc.21334.

42 S. Amamou, H. Lazreg, J. Hafsa, H. Majdoub and C. Rihouey, Effect of extraction condition on the antioxidant , antiglycation and α - amylase inhibitory activities of Opuntia macrorhiza fruit peels polysaccharides, *LWT–Food Sci. Technol.*, 2020, **127**, 109411, DOI: 10.1016/j.lwt.2020.109411.

43 H. Wang, M. Zhang, K. Wei, Y. Zhao and H. Nie, Pyrrolic nitrogen dominated the carbon dot mimic oxidase activity, *Carbon*, 2021, **179**, 692–700, DOI: 10.1016/j.carbon.2021.04.061.

44 H. Ferjani, Structural, Hirshfeld Surface Analysis, Morphological Approach, and Spectroscopic Study of New Hybrid Iodobismuthate Containing Tetranuclear 0D Cluster Bi4I16·4(C6H9N2) 2(H2O), *Crystals*, 2020, **10**, 1–14, DOI: 10.3390/cryst10050397.

45 M. Gassara, R. Msalmi, X. Liu, F. Hassen, A. Moliterni, N. Ben Hamadi, A. Guesmi, L. Khezami, T. Soltani and H. Naïli, A promising 1D Cd-based hybrid perovskite-type for white-light emission with high-color-rendering index, *RSC Adv.*, 2022, **12**, 33516–33524, DOI: 10.1039/d2ra04676h.

46 O. Ucar, I. Ismet and O. Muazzez, Structural and antimicrobial studies of antimony (III) halide complexes with thiophene - based thiosemicarbazones, *Monatsh. Chem.*, 2025, **11**, 1129–1141, DOI: 10.1007/s00706-025-03385-7.

47 L. Mao, P. Guo, R. D. Schaller, C. C. Stoumpos and M. G. Kanatzidis, Structural Diversity in White-Light-Emitting Hybrid Lead Bromide Perovskites, *J. Am. Chem. Soc.*, 2018, (40), 13078–13088, DOI: 10.1021/jacs.8b08691.

48 M. G. Kanatzidis, White-Light Emission and Structural Distortion in New Corrugated Two-Dimensional Lead Bromide Perovskites, *J. Am. Chem. Soc.*, 2017, **139**, 14, DOI: 10.1021/jacs.7b01312.

49 U. A. I. Acharige and G. C. Saunders, The Influence of the Halide in the Crystal Structures of, 1-(2,3,5,6-Tetrafluoro-4-pyridyl)-3-benzylimidazolium Halides, *Molecules*, 2022, 1–11, DOI: 10.3390/molecules27217634.

50 E. R. T. Tiekink, Characterising Supramolecular Architectures in Crystals Featuring I · · · Br Halogen Bonding : Persistence of X · · · X, *Secondary-Bonding in Their Congeners, Crystals*, 2021, **11**(433), DOI: 10.3390/CRYST11040433.

51 I. Warad, F. Al Rimawi, A. Barakat, S. Affouneh and N. Shivalingegowda, Synthesis , spectral , thermal , crystal structure , Hirschfeld analysis of [bis (triamine) Cadimium (II)][Cadimum (IV) tetra - bromide] complexes and their thermolysis to CdO nanoparticles, *Chem. Cent. J.*, 2016, 1–11, DOI: 10.1186/s13065-016-0183-y.

52 M. Hawash, N. Jaradat, S. Shekfeh, M. Abualhasan, A. M. Eid and L. Issa, Molecular docking, chemo-informatic properties, alpha-amylase, and lipase inhibition studies of benzodioxol derivatives, *BMC Chem.*, 2021, **15**, 40, DOI: 10.1186/s13065-021-00766-x.

53 A. Kumar, V. Kumar Singh and A. M. Kayastha, Studies on α-amylase inhibition by acarbose and quercetin using fluorescence, circular dichroism, docking, and dynamics simulations, *Spectrochim. Acta, Part A*, 2024, **314**, 124160, DOI: 10.1016/j.saa.2024.124160.

54 C. Aydın, M. S. A. El-sadek, K. Zheng, I. S. Yahia and F. Yakuphanoglu, Synthesis , diffused reflectance and electrical properties of nanocrystalline Fe-doped ZnO via sol – gel calcination technique, *Opt Laser. Technol.*, 2013, **48**, 447–452, DOI: 10.1016/j.optlastec.2012.11.004.

55 A. Walsh, Principles of Chemical Bonding and Band Gap Engineering in Hybrid Organic – Inorganic Halide Perovskites, *J. Phys. Chem. C*, 2015, **119**, DOI: 10.1021/jp512420b.

56 A. Jacob, O. Jin, K. Park, H. Joon, L. Yunmi, S. David and S. Lee, Metal halide perovskites : a platform for next - generation multifunctional devices, *Advances in Industrial and Engineering Chemistry*, 2025, **1**, 12, DOI: 10.1007/s44405-025-00011-2.

57 Y. Jiang, J. Yin, R. Xi and H. Fei, Chemical Science Promoting the formation of metal – carboxylate coordination to modulate the dimensionality of ultrastable lead halide hybrids, *Chem. Sci.*, 2024, 2848–2856, DOI: 10.1039/d3sc04969h.

58 S. Ye, F. Xiao, Y. X. Pan, Y. Y. Ma and Q. Y. Zhang, Phosphors in phosphor-converted white light-emitting diodes : Recent advances in materials, techniques and properties, *Mater. Sci. Eng., R*, 2010, **71**, 1–34, DOI: 10.1016/j.mser.2010.07.001.

59 (*a*) CCDC 2543017: Experimental Crystal Structure Determination, 2026, DOI: 10.5517/ccdc.csd.cc2rc6t5; (*b*) CCDC 2543018: Experimental Crystal Structure Determination, 2026, DOI: 10.5517/ccdc.csd.cc2rc6v6.